

Insight into the Crystalline Structure of ThF₄ with the Combined Use of Neutron Diffraction, ¹⁹F Magic-Angle Spinning-NMR, and Density Functional Theory Calculations

Martel, Laura; Capelli, Elisa; Body, Monique; Klipfel, Marco; Beneš, Ondrej; Maksoud, Louis; Raison, Phillippe E.; Suard, Emmanuelle; Visscher, Lucas; More Authors

DOI

[10.1021/acs.inorgchem.8b02683](https://doi.org/10.1021/acs.inorgchem.8b02683)

Publication date

2018

Document Version

Final published version

Published in

Inorganic Chemistry

Citation (APA)

Martel, L., Capelli, E., Body, M., Klipfel, M., Beneš, O., Maksoud, L., Raison, P. E., Suard, E., Visscher, L., & More Authors (2018). Insight into the Crystalline Structure of ThF₄ with the Combined Use of Neutron Diffraction, ¹⁹F Magic-Angle Spinning-NMR, and Density Functional Theory Calculations. *Inorganic Chemistry*, 57(24), 15350-15360. <https://doi.org/10.1021/acs.inorgchem.8b02683>

Important note

To cite this publication, please use the final published version (if applicable).
Please check the document version above.

Copyright

Other than for strictly personal use, it is not permitted to download, forward or distribute the text or part of it, without the consent of the author(s) and/or copyright holder(s), unless the work is under an open content license such as Creative Commons.

Takedown policy

Please contact us and provide details if you believe this document breaches copyrights.
We will remove access to the work immediately and investigate your claim.

Insight into the Crystalline Structure of ThF₄ with the Combined Use of Neutron Diffraction, ¹⁹F Magic-Angle Spinning-NMR, and Density Functional Theory Calculations

Laura Martel,^{*,†} Elisa Capelli,[‡] Monique Body,[§] Marco Klipfel,^{||} Ondrej Beneš,[†] Louis Maksoud,[⊥] Phillipe E. Raison,[†] Emmanuelle Suard,[#] Lucas Visscher,[¶] Catherine Bessada,[⊥] Christophe Legein,^{*,§} Thibault Charpentier,[∇] and Attila Kovács[†]

[†]European Commission, Joint Research Centre (JRC), Postfach 2340, D-76125 Karlsruhe, Germany

[‡]Radiation Science & Technology Department, Nuclear Energy and Radiation Applications (NERA), Delft University of Technology, Mekelweg 15, 2629 JB Delft, The Netherlands

[§]Institut des Molécules et des Matériaux du Mans (IMMM), UMR 6283 CNRS, Le Mans Université, Avenue Olivier Messiaen, 72085 Le Mans Cedex 9, France

^{||}Kerntechnische Entsorgung Karlsruhe GmbH, Hermann-von-Helmholtz-Platz 1, 76344 Eggenstein-Leopoldshafen, Germany

[⊥]CNRS, CEMHTI, UPR 3079, Université d'Orléans, F-45071 Orléans, France

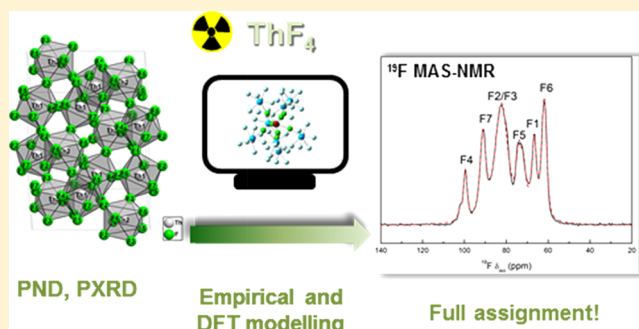
[#]Institut Laue Langevin, 6 Rue Jules Horowitz, BP 156, 38042 Grenoble Cedex 9, France

[¶]Division of Theoretical Chemistry, Vrije Universiteit Amsterdam, De Boelelaan 1083, NL-1081 HV Amsterdam, The Netherlands

[∇]NIMBE, CEA, CNRS, Université Paris-Saclay, CEA Saclay, 91191 Gif-sur-Yvette, France

Supporting Information

ABSTRACT: Because of its sensitivity to the atomic scale environment, solid-state NMR offers new perspectives in terms of structural characterization, especially when applied jointly with first-principles calculations. Particularly, challenging is the study of actinide-based materials because of the electronic complexity of the actinide cations and to the hazards due to their radioactivity. Consequently, very few studies have been published in this subfield. In the present paper, we report a joint experimental–theoretical analysis of thorium tetrafluoride, ThF₄, containing a closed-shell actinide (5f⁰) cation. Its crystalline structure has been revisited in the present work using powder neutron diffraction experiments. The ¹⁹F NMR parameters of the seven F crystallographic sites have been modeled using an empirical superposition model, periodic first-principles calculations, and a cluster-based all-electron approach. On the basis of the atomic position optimized structure, a complete and unambiguous assignment of the ¹⁹F NMR resonances to the F sites has been obtained.



1. INTRODUCTION

As its natural reserves in the Earth's crust are higher than uranium and because of the ease to exploit this resource in many countries, thorium has been considered as a fertile element in several types of existing reactors^{1,2} particularly the molten salt type. In these reactors, fluoride is preferred as a counterion because ¹⁹F is the only stable fluorine isotope and it does not become radioactive under neutron bombardment.³ A further advantage of the thorium fluoride salt, ThF₄, is its dual role in the fuel, serving additionally as a primary coolant in such thorium-based molten salt reactors.⁴

¹⁹F being an NMR-active nucleus, this spectroscopy is well suited to experimentally characterize ThF₄.⁵ Indeed, Bessada et al.⁶ showed an evolution in LiF–ThF₄ melts from free F originating from LiF, to bridging F between ThF_x polyhedra in

melts rich in ThF₄. However, although in the melt, the NMR spectrum was well characterized because of the averaging of the anisotropic interactions (providing one well-resolved ¹⁹F peak at about 125 ppm), the interpretation of the solid-state spectrum was incomplete.⁶ In the solid state, anisotropic interactions lead to a complex magic-angle spinning (MAS)-NMR spectrum characterized by the presence of a “group” of isotropic resonances between 53 and 101 ppm.⁶ A detailed assignment of these resonances to the seven F sites of the crystalline structure determined from single-crystal X-ray diffraction (SCXRD)⁷ was not performed. In addition, the ¹⁹F spectrum of ThF₄ presents an intense pattern of spinning

Received: September 20, 2018

Published: November 26, 2018

sidebands because of strong chemical shift anisotropy (CSA) as those of isostructural β -ZrF₄ and CeF₄.⁸ We note that among the few NMR studies done on actinide fluorides,^{6–12} only two reports high-resolution solid-state NMR.^{6,12}

Fortunately, assistance for the interpretation of NMR experiments can be obtained from theory. Because of recent advances in first-principles modeling techniques, particularly in density functional theory (DFT), it is now possible to calculate efficiently the NMR parameters in crystalline materials.^{13–15} The gauge including projector augmented wave (GIPAW)^{16,17} approach using periodic boundary conditions has been applied to numerous chemical systems including inorganic fluorides for the assignment of ¹⁹F resonances.^{18–20} However, hitherto, only a few studies have been published on the description of the NMR parameters of actinide-based materials in the solid state.^{12,21–24} Their understanding is particularly challenging because of the numerous electrons involved even in the simplest cases like the closed-shell uranium cation (5f⁰). The complexity only further increases with open-shell cations for which very recent quantum chemical calculations were performed on organometallic complexes.^{25–27}

The main goal of the present study is to have a better understanding of the NMR parameters of ThF₄ (5f⁰) using a joint experimental–theoretical analysis. First, the sample was carefully synthesized with all of the precautions required for this type of air-sensitive and radioactive material,^{28,29} and its crystalline purity was checked by powder X-ray diffraction (PXRD). A precise refinement of the crystalline structure parameters was then possible thanks to powder neutron diffraction (PND) which offers a greater sensitivity than PXRD for the F atom detection which are much lighter than the thorium atoms. This step is indeed required to obtain a solid basis for accurate calculation of NMR parameters and reliable assignment of the ¹⁹F NMR resonances to the crystallographic sites. Second, the ¹⁹F MAS-NMR spectrum of the sample was recorded at a high spinning rate to avoid overlapping between the isotropic peaks and the spinning sidebands. Finally, three approaches were applied to obtain the full assignment of the ¹⁹F NMR peaks to the F sites. In the first part, an empirical calculation of the ¹⁹F isotropic chemical shift (δ_{iso}) was done by applying the superposition model (SM)³⁰ which has been successful for such purpose in β -ZrF₄ and CeF₄.⁸ In the second part, the ¹⁹F shielding tensors (σ) were computed under periodic boundary conditions using the GIPAW method^{16,17} implemented in the CASTEP code.^{31,32} This type of calculations are currently most widely applied for structural characterization of solid-state materials. It allows to predict the ¹⁹F isotropic shielding values (σ_{iso}) as well as the three orthogonal principal components of the shielding tensor (σ_{11} , σ_{22} , and σ_{33}). These empirical and first-principles calculations were carried out on the experimental structure (ES) and atomic position optimized (APO) PND structure. In the third and last part, the ¹⁹F σ_{iso} values were calculated using a cluster model by means of the Amsterdam density functional (ADF) package.^{33,34} Such DFT calculations have been proven to be efficient to predict the δ_{iso} values in fluorine-based materials.^{35,36} The main advantage of this approach is the possibility to assess the spin–orbit (SO) effect which is not yet available in the solid-state codes. This effect was shown to play some role for σ_{iso} of other actinide-based materials.^{24,37} All of these approaches provided a consistent interpretation of the thorium tetrafluoride's ¹⁹F MAS-NMR spectrum.

2. EXPERIMENTAL SECTION

2.1. Synthesis. The preparation of highly pure actinide fluorides is a challenging procedure as compounds such as ThF₄ or UF₄ are moisture- and oxygen-sensitive and are likely to contain oxide and oxyfluoride impurities. As for PND, the sample needed to be produced in the gram scale, and the fluorination facility available at JRC-Karlsruhe was used. The synthesis is based on the solid–gas reaction involving stoichiometric ThO₂ and HF gas: ThO₂(s) + 4HF(g) → ThF₄(s) + 2H₂O(g). The HF gas was flushed through the fluorination reactor during about 2 h at 873.15 K. More details about the synthesis are given in the ref 38. The purity of the sample was checked using the differential scanning calorimetry method for the identification of melting point ($T = 1383$ K) which was found to be in very close agreement with the previously published data.^{29,39} Powders from this batch were also used for PXRD and MAS-NMR characterization.

2.2. Powder X-ray and Neutron Diffraction Characterization. The crystal structure of the synthesized compound was first analyzed by PXRD using a Bruker D8 Advance diffractometer mounted in a Bragg–Brentano configuration with a curved Ge monochromator (111), a copper tube (40 kV, 40 mA), and equipped with a LynxEye position sensitive detector. The data were collected by step scanning using a step size of 0.0092° in the angle range 10° ≤ 2θ ≤ 120°. The sample preparation for PXRD analysis consisted of dispersing the powder on the surface of a silicon wafer with 2 or 3 drops of isopropanol.

The PND experiment was performed at 300 K on the instrument D2B of the Institut Laue Langevin (ILL) with 0.81 g of the material. The sample was encapsulated under He in a hermetic vanadium container. The data were collected at a fixed wavelength ($\lambda = 1.594$ Å) in the angle range 0° ≤ 2θ ≤ 160°. Each step corresponded to 0.05° in 2θ as the 128 detectors are spaced at 1.25° intervals. Structural analyses were performed with the Rietveld method by means of the Fullprof2k suite⁴⁰ using the scattering lengths of the elements (Th: 10.31 fm; F: 5.654 fm). Crystallographic data (excluding structure factors) for the structure of ThF₄ have been deposited at the Cambridge Crystallographic Data Centre (CCDC 1868671).

2.3. Solid-State NMR Spectroscopy. All ¹⁹F MAS NMR spectra were recorded on a 9.4 T spectrometer with a commercial ultrafast 1.3 mm probe embedded in a radioactive glovebox.⁴¹ The one-pulse ¹⁹F MAS-NMR experiments were carried out at two spinning frequencies (40 and 60 kHz). The 90° pulse length was set to 1.5 μs (corresponding to a nutation frequency of ~170 kHz) and the recycling delay to 1000 s in order to acquire quantitative spectra. All spectra were referenced to NaF, as a secondary reference to CFCl₃, with a chemical shift at –224.2 ppm.⁴² Because of air frictional heating, the sample temperature varies from 321 K at 40 kHz to 336 K at 60 kHz. The ¹⁹F MAS-NMR spectra were fitted using the Dmfit software.⁴³

2.4. Theoretical Calculations. Diagonalization of the symmetric part of the shielding tensor (σ) yields three orthogonal principal components (σ_{ii}), σ_{11} , σ_{22} , and σ_{33} , defining the isotropic shielding as $\sigma_{\text{iso}} = (\sigma_{11} + \sigma_{22} + \sigma_{33})/3$ with the σ_{ii} in the sequence $|\sigma_{33} - \sigma_{\text{iso}}| \geq |\sigma_{11} - \sigma_{\text{iso}}| \geq |\sigma_{22} - \sigma_{\text{iso}}|$.^{44–46} The principal components of the chemical shift tensor (δ_{ii}), δ_{11} , δ_{22} , and δ_{33} , are related to σ_{11} , σ_{22} , and σ_{33} , respectively, by the linear relation $\delta_{ii} = -\sigma_{ii} + \sigma_{\text{ref}}$ where σ_{ref} is the reference shielding and δ_{iso} defined as $\delta_{\text{iso}} = (\delta_{11} + \delta_{22} + \delta_{33})/3$, is related to σ_{iso} by the linear relation $\delta_{\text{iso}} = -\sigma_{\text{iso}} + \sigma_{\text{ref}}$. For ¹⁹F, linear correlations between calculated σ_{iso} and experimental δ_{iso} values have been established in most cases by refining both the slope and σ_{ref} values.^{12,18,20,42,47–49} The shielding anisotropy, σ_{csa} and the asymmetry parameter, η_{csa} are defined as $\sigma_{\text{csa}} = \sigma_{33} - \sigma_{\text{iso}}$ and $\eta_{\text{csa}} = (\sigma_{22} - \sigma_{11})/\sigma_{\text{csa}}$. The CSA, δ_{csa} , and the asymmetry parameter, η_{csa} , are defined as $\delta_{\text{csa}} = \delta_{33} - \delta_{\text{iso}}$ and $\eta_{\text{csa}} = (\delta_{22} - \delta_{11})/\delta_{\text{csa}}$.

Solid-state DFT calculations of the ¹⁹F σ were performed using the CASTEP code^{31,32} implemented in the Materials Studio 5.0 environment using the GIPAW^{16,17} method. The Perdew–Burke–Ernzerhof functional was employed in the generalized gradient approximation (GGA)⁵⁰ for the exchange–correlation energy, and the

core–valence interactions were described by ultrasoft pseudopotentials (USPPs).¹⁷ The USPPs were generated using the “on the fly” generator (OTF_USPP) included in CASTEP. For ¹⁹F, a core radius of 1.4 au was used with 2s and 2p valence orbitals, whereas for Th, a core radius of 2.0 au was applied with 6s, 6p, 7s, and 6d valence orbitals. The wave functions were expanded on a plane-wave basis set with a kinetic energy cutoff of 700 eV. The Brillouin zone was sampled using a Monkhorst–Pack grid spacing of 0.03 Å⁻¹ (corresponding to a *k*-point mesh of 4 × 4 × 4 in the primitive cell). Atomic positions were optimized by minimizing the residual forces on the atoms down to 10 meV·Å⁻¹ using the Broyden–Fletcher–Goldfarb–Shanno method⁵¹ while keeping symmetry constraints and fixing cell parameters to the experimentally measured values.

For the cluster model, ¹⁹F σ calculations were performed with the ADF code.^{33,34} In these all-electron relativistic DFT calculations, the scalar (SF) and SO relativistic effects were accounted by utilizing the zeroth-order regular approximation (ZORA).⁵² The SAOP exchange–correlation potential^{53,54} was applied, in combination with an uncontracted set of Slater-type orbitals (STOs). Because of the large size of the model cluster, the basis set had to be limited to double-zeta (DZ) quality. The frozen-core approximation was switched off in order to allow a fully all-electron treatment of the system. An auxiliary set of s, p, d, f, and g STOs were used to fit the molecular density and to represent the Coulomb and exchange potentials accurately in each SCF cycle. The closed-shell system was treated using the spin-restricted formalism.

To see the effect of the basis set truncation on the ¹⁹F δ_{iso} values of ThF₄, test calculations were performed with the following basis sets optimized for use with ZORA:⁵⁵ DZ, triple-zeta with one polarization function, triple-zeta with two polarization functions, and quadruple-zeta with four polarization functions (QZ4P). These test calculations were carried out on four Th–F distances, viz., 2.12, 2.29, 2.33, and 2.35 Å. The DZ basis set underestimates the ¹⁹F δ_{iso} values with respect to QZ4P by ca. 20 ppm. However, the results show systematic errors in the ¹⁹F δ_{iso} upon basis set truncation, indicating that for studies of different interatomic distances within the same model structure, smaller basis sets can also be used. A graph demonstrating the dependence of the ¹⁹F δ_{iso} values on the Th–F distance as well as on the size of basis set is given in the Supporting Information (Figure S1).

3. RESULTS AND DISCUSSION

3.1. Crystalline Structure. ThF₄ crystallizes in the monoclinic system with the space group C2/c (no. 15), and its crystallographic structure has been previously determined from SCXRD (ICSD⁵⁶ file number 66009).⁷ To characterize our synthesized compound, we first recorded the PXRD diffraction pattern (Figure S2) and extracted by Rietveld analysis the cell parameters (Table 1) and the atomic positions. The *b* cell parameter slightly differs with the one determined from SCXRD⁷ (11.120 Å) by ~0.1 Å. As the atomic positions are relatively similar to ours, we highly suspect a typing error. On the other hand, the obtained cell parameters are in good agreement with the ones previously determined using PND.⁵⁷ In the later study,⁵⁷ atomic positions have not been reported. We then performed a PND experiment to extract the atomic position of the F atoms more accurately than it can be done by PXRD. Indeed, in the presence of heavy elements, atomic positions of light atoms such as fluorine are not always accurately determined by PXRD because of the large difference in the atomic form factors of the light and heavy atoms. The analyzed PND pattern is presented in Figure 1; the crystallographic data, the fractional atomic coordinates, and the F–Th bond lengths are reported in Tables 1, 2, and 3, respectively. Because of their greatest accuracy, the cell parameters determined by PXRD have been used for the

Table 1. Crystallographic Data from the Rietveld Refinement of the PND Pattern of ThF₄^{a,b}

<i>a</i>	13.043(2) Å
<i>b</i>	11.010(2) Å
<i>c</i>	8.534(2) Å
β	126.31(1)°
<i>V</i>	987.56(1) Å ³
space group	C2/c (no. 15)
<i>Z</i>	2
refined parameters	30
<i>R</i> _{wp}	10.6%
<i>R</i> _p	11.2%
<i>R</i> _B	7.01%
<i>R</i> _{exp}	3.14%
GOF	3.3

^a*R*_p = $\sum [y_i(\text{obs}) - y_i(\text{calc})] / \sum y_i(\text{obs})$; *R*_{wp} = $\{\sum w_i [y_i(\text{obs}) - y_i(\text{calc})]^2 / \sum y_i(\text{obs})\}^{1/2}$. ^b*R*_B = $\sum [I_{hkl}(\text{obs}) - I_{hkl}(\text{calc})] / \sum I_{hkl}(\text{obs})$; GOF = *R*_{wp}/*R*_{exp}.

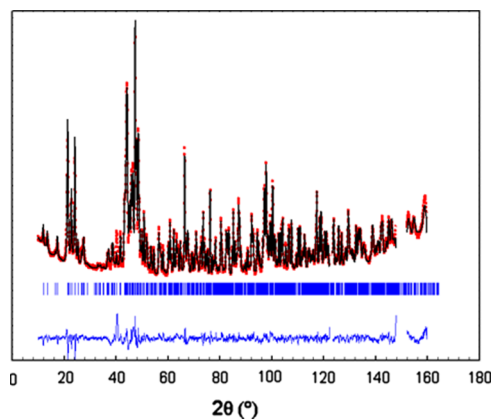


Figure 1. Experimental (red dots) and calculated (black line) room-temperature PND Rietveld refinement patterns of ThF₄ ($\lambda = 1.594$ Å). The Bragg positions (blue vertical ticks) and the difference curve between the experimental and calculated data (bottom blue line) are shown. As a vanadium container was used, the area around $2\theta = 150^\circ$ was deleted to exclude its Bragg reflexion from the Rietveld refinement.

Table 2. Wyckoff Position, Fractional Atomic Coordinates (*x*, *y*, *z*), and Isotropic Displacement Parameters (*B*_{iso}, Å²) from the Rietveld Refinement of the PND Pattern of ThF₄

atom	Wyckoff	<i>x</i>	<i>y</i>	<i>z</i>	<i>B</i> _{iso}
Th1	8f	0.2057(6)	0.4278(6)	0.3323(9)	0.66(6)
Th2	4e	0	0.7869(7)	1/4	0.6(1)
F1	4e	1/2	0.894(1)	1/4	1.9(3)
F2	8f	0.118(1)	0.620(1)	0.282(2)	1.8(2)
F3	8f	0.126(1)	0.846(1)	0.154(1)	1.0(2)
F4	4d	1/4	3/4	0	1.4(3)
F5	8f	0.879(1)	0.948(1)	0.044(2)	1.6(2)
F6	8f	0.891(1)	0.706(1)	0.929(2)	1.2(2)
F7	8f	0.206(1)	0.529(1)	0.098(1)	1.6(2)

analysis of the neutron diffraction data. Because the combination of our PXRD and PND data gave the most relevant structural results, they have been used in the following discussion.

The crystalline structure consists of a three-dimensional network of corner-sharing ThF₈ square antiprisms (SAPs),

Table 3. Individual, Average, and Standard Deviation (σ) Values of F–Th Bond Lengths (Å) from the ES and APO, Difference between F–Th Bond Lengths from ES and APO Structures ($\Delta(\text{F–Th})$), for Each F Site, Sum of These Differences ($\Sigma\Delta(\text{F–Th})$) and, for the Involved F Sites, Absolute Values (with Their Average) of the Difference between Individual F–Th Bond Lengths ($|\Delta(\text{F–Th})|$) from the ES and APO Structures

F site	Th site	count	F–Th		$\Delta(\text{F–Th})$	$\Sigma\Delta(\text{F–Th})$	$ \Delta(\text{F–Th}) $	
			ES	APO			ES	APO
F7	Th1	1×	2.292	2.286	0.006	−0.008	0.022	0.042
	Th1	1×	2.314	2.328	−0.014			
F6	Th1	1×	2.327	2.336	−0.009	0.000	0.060	0.043
	Th2	1×	2.387	2.379	0.009			
F5	Th2	1×	2.325	2.321	0.005	−0.011	0.006	0.026
	Th1	1×	2.331	2.347	−0.015			
F3	Th2	1×	2.311	2.315	−0.003	−0.011	0.010	0.014
	Th1	1×	2.321	2.328	−0.007			
F2	Th2	1×	2.311	2.315	−0.004	−0.011	0.008	0.011
	Th1	1×	2.319	2.326	−0.007			
F4	Th1	2×	2.288	2.293	−0.005	−0.010	0.021	0.027
	Th1	2×	2.367	2.354	0.013			
			$\langle\text{F–Th}\rangle$	2.324	2.327	$\langle\Delta(\text{F–Th})\rangle$		
			$\sigma(\text{F–Th})$	0.027	0.024			

Figure 2). Each F atom is coordinated by two metal atoms. The structure contains two Th and seven F inequivalent

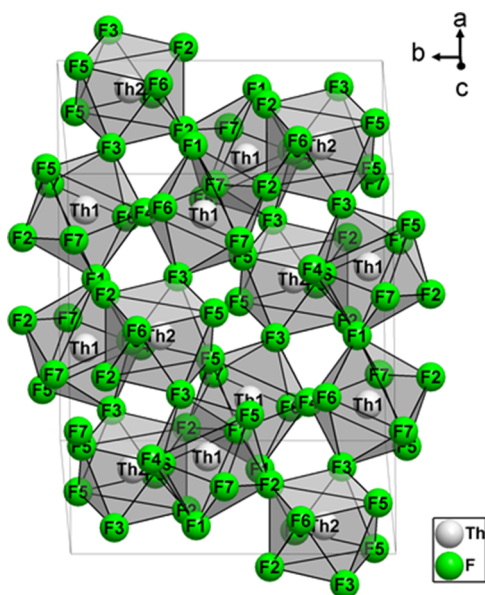


Figure 2. Perspective view of the ThF_8 structure showing the ThF_8 SAPs.

crystallographic sites. Among these seven F sites, two (F1 and F4) have a multiplicity of 4 and the remaining five a multiplicity of 8. Seven resonances among which two with relative intensities equal to 8.3% and five with relative intensities equal to 16.7% are then expected in the ^{19}F MAS-NMR spectra.

For a SAP based on equal edge lengths (hard sphere model) and all metal–ligand bond lengths equal to d_0 , α , the angle that the eight metal–ligand bonds make with the fourfold axis, is equal to 59.3° , α' , the angle between metal–ligand bonds for adjacent ligands, is equal to 74.9° , α'' , the angle between metal–ligand bonds for opposite ligands, is equal to 141.6° , and the edge length is $1.216d_0$ (Figure 3). However, the stereochemistry of the SAP calculated by minimization of the

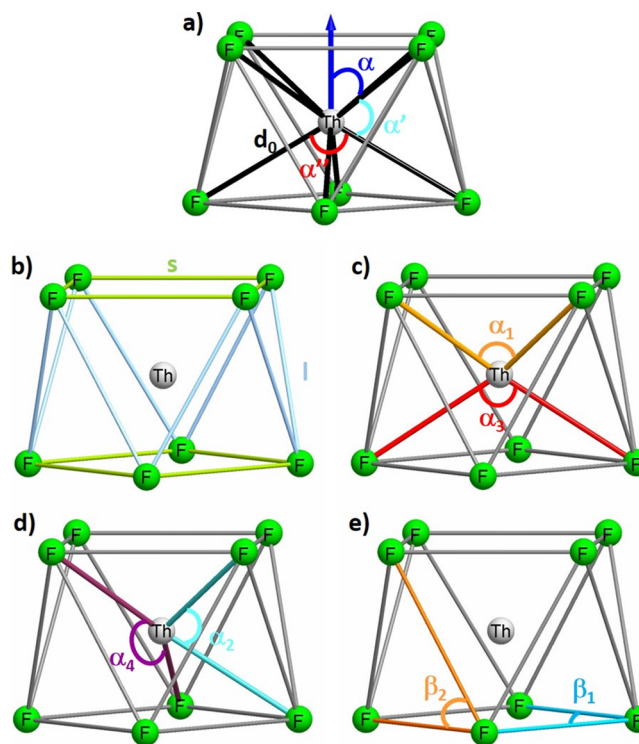


Figure 3. (a) ThF_8 SAP based on equal edge lengths. d_0 is the Th–F bond length, α is the angle the eight Th–F bonds made with the fourfold axis (in blue), α' and α'' are the angles between Th–F bonds for adjacent and opposite F atoms, respectively. (b–e) ThF_8 SAP elongated along the fourfold axis. (b) Edges s and l , joining two adjacent F atoms belonging to the same square face and to different square faces, respectively. (c) F–Th–F angles for adjacent (α_1) and for opposite (α_3) F atoms belonging to the same square face. (d) F–Th–F angles for adjacent (α_2) and for opposite (α_4) F atoms belonging to different square faces. (e) F–F–F angles for three F atoms belonging to the same square face (β_1) and to the same triangular face (β_2).

repulsion energy is elongated along the fourfold axis, $\alpha = 57.1^\circ$, with a contraction of the square faces.⁵⁸ This is observed in ThF_4 as shown (Figure 3 and Table 4) by (i) the average F–

Table 4. Average and Standard Deviation (σ) Values of the F–Th Bond Lengths (Å), of Edge Lengths (F–F Distances, Å) Joining Two Adjacent F Atoms Belonging to the Same Square Face (s) and to Different Square Faces (l), of F–Th–F Angles (deg) for Adjacent F Atoms ($\alpha_{1,2}$) Belonging to the Same Square Face (α_1) and to Different Square Faces (α_2) and for Opposite F Atoms Belonging to the Same Square Face (α_3) and to Different Square Faces (α_4) and of F–F–F Angles (deg) for Three F Atoms Belonging to the Same Square Face (β_1) and to the Same Triangular Face (β_2), for Each ThF₈ SAP, from the ES and APO PND Structures^a

ThF ₈ SAP structure	Th ₁ F ₈		Th ₂ F ₈	
	ES	APO	ES	APO
$\langle \text{Th–F} \rangle$	2.318	2.325	2.338	2.332
$\sigma(\text{Th–F})$	0.023	0.022	0.030	0.027
$\langle s \rangle$	2.781	2.786	2.793	2.793
$\sigma(s)$	0.078	0.086	0.065	0.065
$\langle l \rangle$	2.891	2.903	2.920	2.901
$\sigma(l)$	0.134	0.119	0.074	0.060
$\langle \text{F–F} \rangle$	2.836	2.844	2.857	2.847
$\sigma(\text{F–F})$	0.123	0.119	0.094	0.083
$\langle \text{F–F} \rangle / \langle \text{Th–F} \rangle$	1.224	1.224	1.222	1.221
$\langle \alpha_1 \rangle$	73.7	73.6	73.4	73.6
$\sigma(\alpha_1)$	2.2	2.5	1.9	2.1
$\langle \alpha_2 \rangle$	77.2	77.3	77.3	76.9
$\sigma(\alpha_2)$	4.4	3.9	2.4	2.1
$\langle \alpha_{1,2} \rangle$	75.5	75.5	75.3	75.3
$\sigma(\alpha_{1,2})$	3.9	3.8	3.0	2.7
$\langle \alpha_3 \rangle$	115.5	115.4	115.2	115.7
$\sigma(\alpha_3)$	7.6	7.4	1.2	1.0
$\langle \alpha_4 \rangle$	141.8	141.9	142.2	142.1
$\sigma(\alpha_4)$	4.4	4.5	3.8	3.9
$\langle \beta_1 \rangle$	89.5	89.6	90.0	90.0
$\sigma(\beta_1)$	5.2	5.2	2.5	2.4
$\langle \beta_2 \rangle$	60.0	60.0	60.0	60.0
$\sigma(\beta_2)$	4.0	3.8	2.3	2.0

^aIndividual values are reported in Tables S1–S4.

Th–F angles for opposite F atoms belonging to the same square (α_3) equal to 115.5° and 115.2° for Th₁F₈ and Th₂F₈ SAP, respectively, (ii) the smaller average lengths for edges (s) joining two adjacent F atoms belonging to the same square face (2.781 and 2.793 Å for Th₁F₈ and Th₂F₈ SAP, respectively) than for edges (l) joining two adjacent F atoms belonging to different square faces (2.891 and 2.920 Å for Th₁F₈ and Th₂F₈ SAP, respectively), and (iii) the smaller average F–Th–F angles for adjacent F atoms belonging to the same square face (α_1 , 73.7° and 73.4° for Th₁F₈ and Th₂F₈ SAP, respectively) than to different square faces (α_2 , 77.2° and 77.3° for Th₁F₈ and Th₂F₈ SAP, respectively). Except for the Th–F bond lengths, the standard deviation values of the geometrical parameters of the SAP (Table 4) are smaller for Th₂F₈ which is then overall less distorted than Th₁F₈.

3.2. Atomic Position Optimization Effects. As a result of the high sensitivity of NMR parameters to slight structural modifications, the structural data, on which basis they are computed, should be as accurate and strain-free as possible. Therefore, the crystalline structure is often DFT optimized prior to the calculation of the NMR parameters, and the agreement between the calculated and experimental NMR parameters is usually found to be improved after a DFT

optimization of the geometry.^{13–15,19,20,59,60} For ThF₄, the ES and APO fractional atomic coordinates are compared and the corresponding atomic displacements are given in the Supporting Information (Table S5). In overall, the atomic displacements are small with average Th and F atomic displacements, respectively, equal to 0.018 and 0.022 Å, highlighting the accuracy of the experimental structure and the sensitivity of PND for the (light) F atoms. The average Th–F bond length increases for the Th₁F₈ SAP, whereas it decreases for the Th₂F₈ SAP (Table 4). Consequently, the difference between the average Th–F bond length of Th₁F₈ and Th₂F₈ SAP decreases (from 0.020 to 0.007 Å). The average F–Th bond length slightly increases, and the standard deviation value slightly decreases (Table 3). It seems then somewhat surprising that for F sites with two different F–Th distances, the average of the absolute values of the difference between individual F–Th bond lengths is larger after APO. The difference between individual F–Th bond lengths decreases only for F6 [for which the difference is the largest one (Figure 4)]. The standard deviation values of the s edge lengths slightly

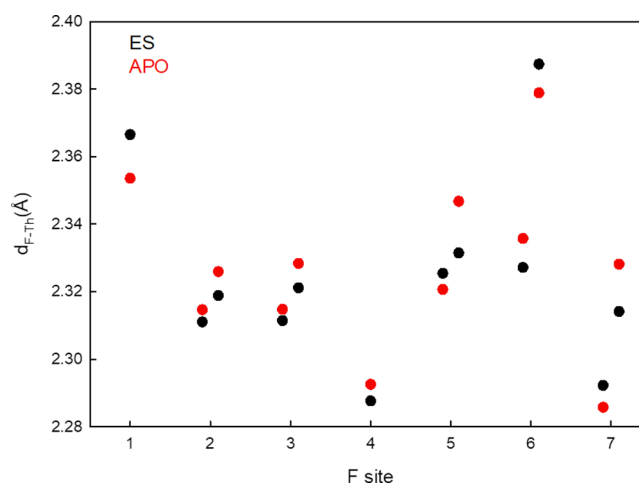


Figure 4. F–Th bond lengths from the ES (black) and APO (red) structures.

increase or remain constant and those of the l edge lengths slightly decrease. Among the four types of F–Th–F angles, the standard deviation values of α_1 and α_4 (α_2 and α_3) increase (decrease). Finally, the standard deviation values of F–F–F angles slightly decrease. Overall, the ThF₈ SAP is then slightly less distorted after APO.

3.3. ¹⁹F MAS-NMR Spectra. The ¹⁹F MAS NMR spectra of ThF₄ acquired at 40 and 60 kHz have been fitted with six ¹⁹F isotropic peaks (Figure 5 and Table 5). No chemical shift or line shape variations have been observed in this range of spinning frequencies or sample temperatures. On the basis of their relative intensities, peaks 1 and 5 are assigned to F1 or F4. The relative intensity of peak 3, equal to 31.6%, corresponds to twice the expected relative intensity for one F site of multiplicity 8 and therefore accounts for two F sites. The three other peaks belong accordingly to the three other F sites with multiplicity 8. An important feature of this spectrum is the strong spinning sideband pattern from which the δ_{csa} and η_{csa} values (Table 5) were determined on the basis of the spinning sideband intensities. The δ_{csa} values are comprised between –237 and –305 ppm. Similar large values were also found for

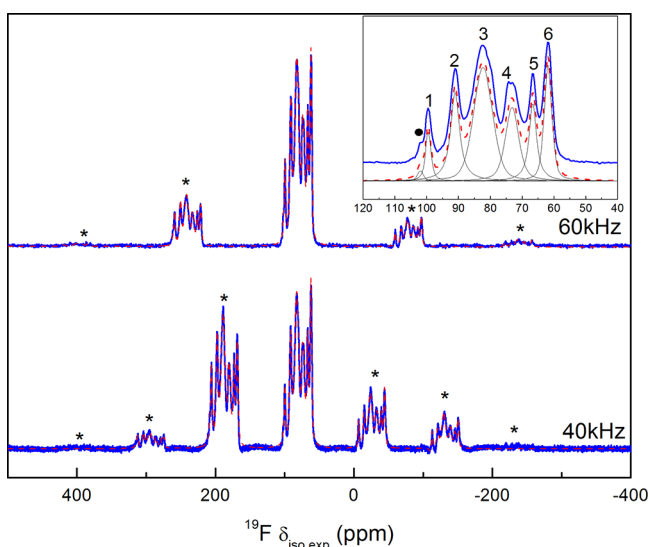


Figure 5. Experimental (blue) and fitted (red dashed) ^{19}F MAS NMR spectra of ThF_4 acquired at 40 and 60 kHz. The stars indicate the spinning sidebands. A zoom on the labeled isotropic peaks of the spectrum recorded at 60 kHz is presented on the inset. The individual contributions to the fitted spectrum are shown below. The filled circle on the inset indicates an impurity.

the isostructural $\beta\text{-ZrF}_4$ (between -160 and -180 ppm) and CeF_4 (between -370 and -410 ppm).⁸

3.4. Empirical Assignment. The SM developed by Bureau et al. for ionic fluorides³⁰ and later extended to more complex systems ($\beta\text{-ZrF}_4$ and CeF_4 ,⁸ compounds from the systems $\text{BaF}_2\text{-AlF}_3$, $\text{CaF}_2\text{-AlF}_3$,⁶¹ and $\text{NaF-CaF}_2\text{-AlF}_3$ ⁵⁹) has been here applied to assign the ^{19}F NMR peaks to the F sites. It considers the ^{19}F δ_{iso} as a sum of a constant diamagnetic term (depending on the chemical shift reference) and several paramagnetic contributions (σ) from the l neighboring cations: $\delta_{\text{iso}}/\text{CFCl}_3 = -291.3 - \sum_l \sigma_l$ with $\sigma_l = \sigma_{l_0} \exp[-\alpha_l(d - d_0)]$. d_0 is the characteristic F–M bond length taken equal to the bond length in the related basic fluoride, and σ_{l_0} determines the order of magnitude of the cationic paramagnetic contribution to the shielding, deduced from measurements in the related basic fluoride where $\delta_{\text{iso}}/\text{CFCl}_3 = -291.3 - n\sigma_{l_0}$.

The initial values of the d_0 , σ_{l_0} , and α_l parameters were determined in the following way. The structure of ThF_4 containing several distinct crystallographic F sites with different F–Th bond lengths and δ_{iso} values, d_0 and σ_{l_0} were calculated considering the weighted average value of the F–Th bond lengths and δ_{iso} values. The α_l parameter has been calculated using its linear relation with, r_l , the crystal radius: $\alpha_l = -0.806r_l + 4.048$, with $r_l = 1.19$ Å for Th^{4+} in eight

coordination.⁶² The obtained d_0 , α_l , and σ_{l_0} initial parameters for the ES and APO structures are given in Table 6.

Table 6. Initial and Refined (in *Italic*) α_l (\AA^{-1}), d_0 (\AA), and σ_{l_0} (ppm) Parameters for the ES and APO Structure

structure	α_l		d_0		σ_{l_0}	
ES	3.089	<i>1.236</i>	2.325	<i>2.326</i>	<i>-185.1</i>	<i>-185.0</i>
APO	3.089	<i>1.524</i>	2.327	<i>2.328</i>	<i>-185.1</i>	<i>-184.8</i>

As done for $\beta\text{-ZrF}_4$ and CeF_4 ,⁸ only the first fluorine coordination spheres ($l = 2$) were considered in these calculations. The δ_{iso} values of the seven F sites obtained with the initial parameters for the ES and APO structures were compared with the experimental results. Assignments were performed, having regard for the partial assignment based on the relative intensities, by minimizing the absolute values of the differences between calculated ($\delta_{\text{iso,cal}}$) and experimental ($\delta_{\text{iso,exp}}$) isotropic chemical shift values: $\Delta\delta_{\text{iso}} = \delta_{\text{iso,exp}} - \delta_{\text{iso,cal}}$. The standard deviation values of $\Delta\delta_{\text{iso}}$ are equal to 17.8 and 12.8 ppm for the ES and APO structures, respectively. For the ES structure, whereas the smallest $\delta_{\text{iso,exp}}$ value corresponds to an F site with multiplicity 8, the smallest $\delta_{\text{iso,cal}}$ value corresponds to F1. Then, the three parameters d_0 , α_l , and σ_{l_0} were refined in order to minimize the difference between $\delta_{\text{iso,exp}}$ and $\delta_{\text{iso,cal}}$ values (i.e., the sum $S = \sum (\delta_{\text{iso,exp}} - \delta_{\text{iso,cal}})^2$). In the usual procedure, a new parameter set is obtained, and, if necessary, the assignments are modified, with respect to the relative intensities, to minimize the $\Delta\delta_{\text{iso}}$ differences. Usually, this process is repeated until the assignments remain unchanged, but in this study, the assignments remained the same with the initial and refined parameters. The ^{19}F $\delta_{\text{iso,cal}}$ values and the peak assignments are collected in Table 7. The

Table 7. F Sites, ^{19}F δ_{iso} Values, Calculated Using the SM, from the ES ($\delta_{\text{iso,cal}}$ ES, ppm) and the APO Structure ($\delta_{\text{iso,cal}}$ APO, ppm) and Assignments to the ^{19}F NMR Peaks

F sites	$\delta_{\text{iso,cal}}$ ES	peak	$\delta_{\text{iso,cal}}$ APO	peak
F4	96.8	1	99.0	1
F7	89.4	2	90.7	2
F2	83.9	3	82.9	3
F3	83.3	3	82.2	3
F5	77.7	4	75.4	4
F1	60.7	6	64.4	5
F6	65.1	5	62.5	6

$\Delta\delta_{\text{iso}}$ standard deviation values decrease drastically, being equal to 3.4 and 1.2 ppm for the ES and APO structures, respectively. Despite the discrepancy mentioned above with

Table 5. ^{19}F Isotropic Chemical Shifts ($\delta_{\text{iso,exp}}$, ppm), CSA (δ_{csa} , ppm), Asymmetry Parameter (η_{csa}), Principal Components of the Chemical Shift Tensor (δ_{ii} , ppm), and Relative Intensity (I , %) of the ^{19}F NMR Resonances of ThF_4

peak	$\delta_{\text{iso,exp}}$ (± 0.5)	δ_{csa} (± 10)	η_{csa} (± 0.10)	δ_{11} (± 10)	δ_{22} (± 10)	δ_{33} (± 10)	I (± 2.0)
1	99.6	-305.0	0.00	252.1	252.1	-205.4	8.2
2	91.1	-270.0	0.10	239.6	212.6	-178.9	17.7
3	82.3	-264.0	0.10	227.5	201.1	-181.7	31.6
4	73.2	-259.7	0.20	229.0	177.1	-186.5	16.2
5	66.6	-252.4	0.39	242.0	143.6	-185.8	10.6
6	61.9	-236.7	0.40	227.6	132.9	-174.8	15.7

the ES structure [due to overestimated F1–Th bond lengths in the ES structure as shown by the differences between F1–Th bond lengths from ES and APO structures (Table 3)], very good linear correlations are observed between the ^{19}F $\delta_{\text{iso,cal}}$ and $\delta_{\text{iso,exp}}$ values (Figure 6). Thus, a complete and convincing

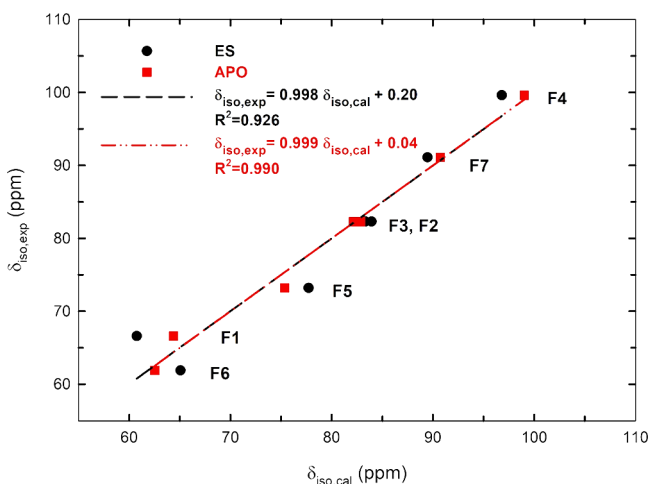


Figure 6. Plot of the ^{19}F experimental isotropic chemical shift ($\delta_{\text{iso,exp}}$) against the ^{19}F empirically calculated isotropic chemical shift ($\delta_{\text{iso,cal}}$) for ThF_4 . The black circles and red squares represent the calculated values from ES and APO structure, respectively. The black dashed line and the red dashed-dotted line represent the linear regressions for the calculated values from ES and APO structures, respectively.

assignment of the ^{19}F NMR peaks is obtained. As previously observed for $\beta\text{-ZrF}_4$ and CeF_4 ,⁸ the only sensitive parameter is α_f and it also decreases for ThF_4 (Table 6). This decrease of α_f , which describes the behavior of the paramagnetic contribution with the fluorine–metal distance, may be correlated with the deviation from the purely ionic model⁶¹ for F–Th bonds.

3.5. Modeling ^{19}F δ_{iso} Using DFT under Periodic Boundary Conditions. To confirm the empirical assignments, we performed ^{19}F shielding tensor calculations using the GIPAW method on both the ES and APO structures. To assign the ^{19}F resonances to the F sites, the F sites were ranked in the increasing order of calculated σ_{iso} values ($\sigma_{\text{iso,cal}}$), the same for both the structures, and NMR lines were ranked in the decreasing order of $\delta_{\text{iso,exp}}$ values. The fine agreement obtained between the relative intensities of the NMR peaks (1, 2, 2, 2, 1, and 2) and the multiplicities (4, 8, 8, 8, 4, and 8) of the F sites (Tables 2, 5, and 8) allows to propose a complete assignment. This assignment perfectly agrees with the

Table 8. F Site, Calculated ^{19}F σ_{iso} Values ($\sigma_{\text{iso,cal}}$, ppm) Using the GIPAW Method from the ES and APO Structure and Assignments to the ^{19}F NMR Peaks

F site	$\sigma_{\text{iso,cal}}$		peak
	ES	APO	
F4	−21.9	−24.5	1
F7	−11.8	−13.6	2
F2	−10.3	−6.1	3
F3	−5.0	−4.5	3
F5	4.3	2.6	4
F1	15.7	9.3	5
F6	18.3	17.9	6

empirical one. Figure 7 presents the plot of the ^{19}F $\delta_{\text{iso,exp}}$ values against the $\sigma_{\text{iso,cal}}$ values. Very good linear correlations

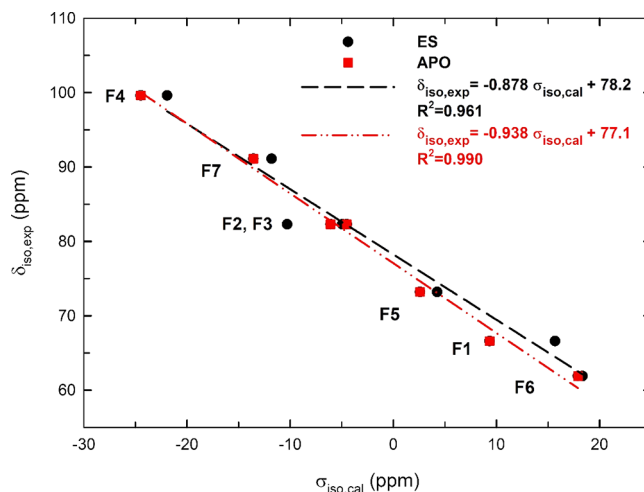


Figure 7. Plot of the experimental ^{19}F isotropic chemical shift ($\delta_{\text{iso,exp}}$) against the GIPAW calculated ^{19}F isotropic chemical shielding ($\sigma_{\text{iso,cal}}$) for ThF_4 determined on the basis of the ES or APO structure. The black circles and red squares represent the calculated values from ES and APO structures, respectively. The black dashed line and the red dashed-dotted line represent the linear regressions for the calculated values from ES and APO structures, respectively.

are determined, especially for the APO structure, confirming its higher accuracy. A strong relationship between ^{19}F σ_{iso} values and accurate F–Th bond lengths is evidenced in ThF_4 . Indeed, ^{19}F δ_{iso} values of the F sites show a strong linear relationship with the sum of the two APO F–Th bond lengths (Figure S3). The slope of the linear regression between ^{19}F $\delta_{\text{iso,exp}}$ and $\sigma_{\text{iso,cal}}$ from the APO structure (−0.938) is close to −1.0, that is, to the theoretical expected value, whereas the slopes of most of the linear regressions established previously from GIPAW calculations^{12,18,20,42,47–49} differ significantly from −1.0. It has been shown that this is caused by the GGA to the exchange–correlation functional, and it is related to the well-known band gap problem.⁶³ The prediction of ^{19}F δ_{iso} values remains a challenge in inorganic fluorides containing atoms sparsely studied. At last, a scaling factor around −0.72 would be necessary to properly reproduce the experimental ^{19}F δ_{csa} values (Table 5) from the calculated ^{19}F σ_{csa} values from the APO structure (Table 9), as shown by the plot (Figure S4) of the experimental δ_{ii} values (Table 5) against the calculated σ_{ii} values (Table 9). As in most of the scarce studies where these

Table 9. Calculated Principal Components of the Shielding Tensor (σ_{11} , σ_{22} , and σ_{33} , ppm), Shielding Anisotropy (σ_{csa} , ppm), and Asymmetry Parameter (η_{csa}) on the Basis of the APO Structure Using the GIPAW Method

F site	σ_{11}	σ_{22}	σ_{33}	σ_{csa}	η_{csa}
F1	−170.4	−167.3	365.7	356.3	0.01
F2	−232.4	−130.0	344.1	350.2	0.29
F3	−225.0	−154.3	365.7	370.2	0.19
F4	−281.4	−170.3	378.3	402.7	0.28
F5	−219.3	−134.2	361.3	358.7	0.24
F6	−184.0	−128.1	365.9	347.9	0.16
F7	−231.1	−159.6	350.0	363.6	0.20

values are compared, the experimental ^{19}F δ_{csa} values of ThF_4 seem then to be underestimated.^{12,20,64,65} Whereas the same slopes are expected between σ_{csa} and δ_{csa} and between σ_{iso} and δ_{iso} , in some cases such as ThF_4 or NbF_5 ,²⁰ both slopes differ. It must only be pointed out that δ_{csa} values are not as accurate as δ_{iso} values.

3.6. ^{19}F σ_{iso} DFT Cluster Calculations and SO Relativistic Effects. In both previous methods, the SO effects are not included. In order to overcome this drawback, which was shown to be of importance in these *5f* systems,^{25,26} we also performed calculations on a cluster model by using the ADF code which includes the facility to account for SO effects. Thus, the ThF_4 crystal was modeled by a central ThF_8 moiety and its first coordination sphere consisting of the next-nearest ThF_8 moieties leading to the cluster Th_9F_{59} (Figure 8). Th being eight-coordinated, the cluster including the second coordination sphere is very large and calculations were, in our case, unfortunately not feasible.

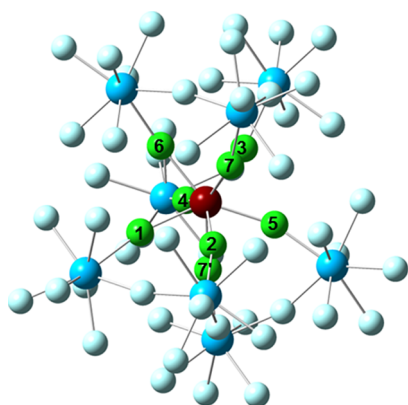


Figure 8. Th_9F_{59} cluster model (Cartesian coordinates given in Table S6) with the central ThF_8 unit indicated with different colors (Th = blue/purple, F = light blue/green).

The ^{19}F σ_{iso} values calculated with the SF and SO relativistic effects are given in Table 10 and plotted against the ^{19}F $\delta_{\text{iso,exp}}$ values in Figure 9. As expected given the atomic number of Th ($Z = 90$), the relativistic effects are significant³⁶ and these ^{19}F σ_{iso} values are larger than those calculated using the GIPAW method. For both the SF and SO levels, these calculations led to $\sigma_{\text{iso,cal}}$ values in the same order than those obtained with the GIPAW method and then to the same assignments. Good

Table 10. Calculated ^{19}F σ_{iso} Values ($\sigma_{\text{iso,cal}}$ ppm) Using the Cluster Th_9F_{59} Constructed on the Basis of the APO Structure and ^{19}F NMR Peak Assignments^a

F site	$\sigma_{\text{iso,cal}}$		peak
	SF	SO	
F4	150.5	139.5	1
F7(F7') ^b	151.1(152.2)	144.4(145.7)	2
F2	162.1	155.8	3
F3	163.4	156.2	3
F5	170.6	162.0	4
F1	174.8	167.6	5
F6	177.9	171.7	6

^aSF and SO acronyms correspond to the scalar and the SO relativistic effects, respectively. ^bThe F7 site appears twice in the central ThF_8 moiety of the model structures as F7 and F7' (see Figure 8).

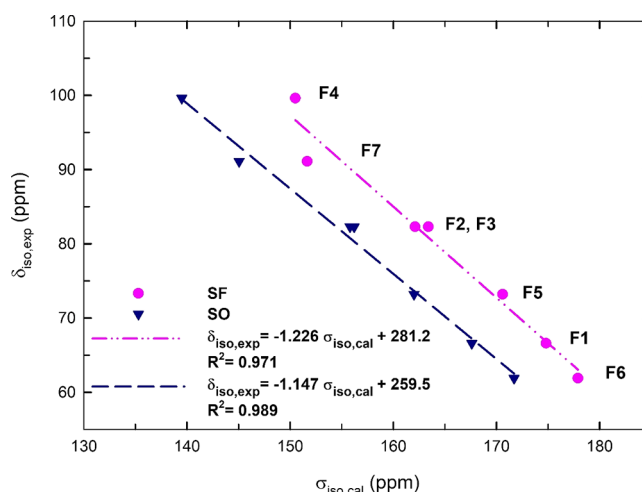


Figure 9. Plot of the experimental ^{19}F isotropic chemical shift ($\delta_{\text{iso,exp}}$) against the calculated ^{19}F isotropic chemical shielding ($\sigma_{\text{iso,cal}}$) at the SAOP/DZ level from the Th_9F_{59} cluster based on the APO structure of ThF_4 . The two data sets were obtained accounting for scalar (SF, purple circles) and in addition for SO (blue triangles) relativistic effects. The pink dashed-dotted line and the blue dashed line represent the linear regressions for the calculated values at the SF and SO relativistic levels, respectively.

$\delta_{\text{iso,exp}}$ versus $\sigma_{\text{iso,cal}}$ linear correlations are obtained (R^2 values equal to 0.971 and 0.989, respectively). The $\delta_{\text{iso,exp}}$ versus $\sigma_{\text{iso,cal}}$ linear regressions have slopes inferior to -1 , which is unusual using the GIPAW method.^{12,18,48,49} Considering the SO effect improves the quality of the computed data and leads to a decrease of the ^{19}F σ_{iso} by 6.1–11.0 ppm. The largest effect is observed for the smallest σ_{iso} belonging to F4 (11 ppm), which has the smallest F–Th bond lengths (Table 3 and Figure 4). The other F sites change by 6.1–8.4 ppm upon SO. This relatively small effect on the light atom shielding due to the influence of the heavy atom SO coupling indicates that SO coupling in Th is largely quenched and lends support for the use of the models used above.

4. CONCLUSIONS

The crystalline structure of ThF_4 has been revised using PND experiments. It consists of a three-dimensional network of corner-sharing ThF_8 SAP. The ^{19}F MAS-NMR spectrum presents six ^{19}F isotropic peaks, ranging within ~ 40 ppm, partially assigned to the seven F crystallographic sites, on the basis of their relative intensities. Although the effects of the crystalline structure optimization are small and highlight the accuracy of the experimental structure, they slightly improve the linear correlation between $\delta_{\text{iso,exp}}$ and $\sigma_{\text{iso,cal}}$ values. All three approaches (i.e., empirical model, periodic first-principles calculations, and a cluster-based all-electron approach) employed for modeling the ^{19}F NMR parameters positively agree on a single, complete, and convincing assignment of the ^{19}F NMR peaks corresponding to the seven inequivalent F sites. Indeed, peaks 1, 2, 3, 4, 5, and 6 can be attributed to F4, F7, F2/F3, F5, F6, and F1, respectively. In addition, we have shown that there was only a small effect of the SO coupling which is encouraging for the use of solid-state codes in such $5f^0$ -based materials. The present work is a solid basis to further study structure–property relations of this actinide-based material.

■ ASSOCIATED CONTENT

Supporting Information

The Supporting Information is available free of charge on the ACS Publications website at DOI: 10.1021/acs.inorgchem.8b02683.

Variation of the ^{19}F σ_{iso} values determined using the ADF code with F–Th distance and with the size of the basis set, PXRD Rietveld refinement patterns of ThF_4 , additional structural features about the ThF_8 SAP, fractional atomic coordinates from ES and APO NPD structures of ThF_4 , corresponding atomic displacements, plot of the ^{19}F δ_{iso} values versus the sum of the two APO F–Th bond lengths, and plot of ^{19}F δ_{ii} values versus calculated ^{19}F σ_{ii} values from APO structure and Cartesian coordinates of the Th_9F_{59} cluster (PDF)

Accession Codes

CCDC 1868671 contains the supplementary crystallographic data for this paper. These data can be obtained free of charge via www.ccdc.cam.ac.uk/data_request/cif, or by emailing data_request@ccdc.cam.ac.uk, or by contacting The Cambridge Crystallographic Data Centre, 12 Union Road, Cambridge CB2 1EZ, UK; fax: +44 1223 336033.

■ AUTHOR INFORMATION

Corresponding Authors

*E-mail: laura.martel@ec.europa.eu (L.M.).

*E-mail: christophe.legein@univ-lemans.fr (C.L.).

ORCID

Laura Martel: 0000-0001-8554-2711

Lucas Visscher: 0000-0002-7748-6243

Christophe Legein: 0000-0001-7426-8817

Thibault Charpentier: 0000-0002-3034-1389

Attila Kovács: 0000-0001-8169-3547

Author Contributions

The manuscript was written through contributions of all authors. All authors have given approval to the final version of the manuscript.

Notes

The authors declare no competing financial interest.

■ ACKNOWLEDGMENTS

L.M. acknowledges C. Selfslag for his support with the NMR spectrometer, D. Bouxière for the acquisition of the XRD pattern; A. Rakhmatullin, F. Fayon, R. Eloiird, and J. Somers for fruitful discussions. E.C. and O.B. acknowledge P. Souček for his support for synthesizing the material. C.L. and M.B. acknowledge M. Biswal for preliminary work on ThF_4 during her PhD thesis. The GIPAW computations presented in this work have been carried out at the Centre Régional de Calcul Intensif des Pays de la Loire (CCIPL), financed by the French Research Ministry, the Région Pays de la Loire, and Nantes University. We thank CCIPL for the CASTEP licenses financial support. M.K. thanks Prof. F. M. Bickelhaupt for a two-week stay at the Vrije Universiteit Amsterdam.

■ REFERENCES

- (1) Lung, M.; Gremm, O. Perspectives of the thorium fuel cycle. *Nucl. Eng. Des.* **1998**, *180*, 133–146.
- (2) Peng, Y.; Zhu, G.; Zou, Y.; Liu, Y.; Yu, X.; Cai, X.; Xu, H. The feasibility research of thorium breeding using fluoride salt as a fast reactor coolant. *Prog. Nucl. Energy* **2017**, *101*, 199–208.

- (3) Serp, J.; Allibert, M.; Beneš, O.; Delpech, S.; Feynberg, O.; Ghetta, V.; Heuer, D.; Holcomb, D.; Ignatiev, V.; Kloosterman, J. L.; Luzzi, L.; Merle-Lucotte, E.; Uhlir, J.; Yoshioka, R.; Zhimin, D. The molten salt reactor (MSR) in generation IV: Overview and perspectives. *Prog. Nucl. Energy* **2014**, *77*, 308–319.

- (4) Delpech, S.; Merle-Lucotte, E.; Heuer, D.; Allibert, M.; Ghetta, V.; Le-Brun, C.; Doligez, X.; Picard, G. Reactor physic and reprocessing scheme for innovative molten salt reactor system. *J. Fluorine Chem.* **2009**, *130*, 11–17.

- (5) Gabuda, S. P.; Gagarinskii, Y. V.; Lundin, A. G. Nuclear magnetic resonance and electron structure of uranium, thorium, and zirconium tetrafluorides. *J. Struct. Chem.* **1967**, *7*, 192–198.

- (6) Bessada, C.; Rakhmatullin, A.; Rollet, A.-L.; Zanghi, D. Lanthanide and actinide speciation in molten fluorides: A structural approach by NMR and EXAFS spectroscopies. *J. Nucl. Mater.* **2007**, *360*, 43–48.

- (7) Benner, G.; Müller, B. G. Zur Kenntnis binärer Fluoride des ZrF_4 -Typs: HfF_4 und ThF_4 . *Z. Anorg. Allg. Chem.* **1990**, *588*, 33–42.

- (8) Legein, C.; Fayon, F.; Martineau, C.; Body, M.; Buzaré, J.-Y.; Massiot, D.; Durand, E.; Tressaud, A.; Demourgues, A.; Péron, O.; Boulard, B. ^{19}F High Magnetic Field NMR Study of β - ZrF_4 and CeF_4 : from Spectra Reconstruction to Correlation between Fluorine Sites and ^{19}F Isotropic Chemical Shifts. *Inorg. Chem.* **2006**, *45*, 10636–10641.

- (9) Capan, C.; Dempsey, R. J.; Sinkov, S.; McNamara, B. K.; Cho, H. Probing the Pu^{4+} magnetic moment in PuF_4 with ^{19}F NMR spectroscopy. *Phys. Rev. B: Condens. Matter Mater. Phys.* **2016**, *93*, 224409.

- (10) Gabuda, S. P.; Falaleeva, L. G.; Gagarinskii, Y. V. Dipolar broadening of the NMR spectrum of ^{19}F in UF_4 . *Phys. Status Solidi B* **1969**, *33*, 435–438.

- (11) Pintar, M. NMR evidence for contact hyperfine coupling in paramagnetic UF_4 . *Phys. Status Solidi B* **1966**, *14*, 291–295.

- (12) DeVore, M. A.; Klug, C. A.; Kriz, M. R.; Roy, L. E.; Wellons, M. S. Investigations of Uranyl Fluoride Sesquihydrate ($\text{UO}_2\text{F}_2 \cdot 1.57\text{H}_2\text{O}$): Combining ^{19}F Solid-State MAS NMR Spectroscopy and GIPAW Chemical Shift Calculations. *J. Phys. Chem. A* **2018**, *122*, 6873–6878.

- (13) Charpentier, T. The PAW/GIPAW approach for computing NMR parameters: A new dimension added to NMR study of solids. *Solid State Nucl. Magn. Reson.* **2011**, *40*, 1–20.

- (14) Bonhomme, C.; Gervais, C.; Babonneau, F.; Coelho, C.; Pourpoint, F.; Azais, T.; Ashbrook, S. E.; Griffin, J. M.; Yates, J. R.; Mauri, F.; Pickard, C. J. First-Principles Calculation of NMR Parameters Using the Gauge Including Projector Augmented Wave Method: A Chemist's Point of View. *Chem. Rev.* **2012**, *112*, 5733–5779.

- (15) Ashbrook, S. E.; McKay, D. Combining solid-state NMR spectroscopy with first-principles calculations - a guide to NMR crystallography. *Chem. Commun.* **2016**, *52*, 7186–7204.

- (16) Pickard, C. J.; Mauri, F. All-electron magnetic response with pseudopotentials: NMR chemical shifts. *Phys. Rev. B: Condens. Matter Mater. Phys.* **2001**, *63*, 245101.

- (17) Yates, J. R.; Pickard, C. J.; Mauri, F. Calculation of NMR Chemical Shifts for Extended Systems using Ultrasoft Pseudopotentials. *Phys. Rev. B: Condens. Matter Mater. Phys.* **2007**, *76*, 024401.

- (18) Griffin, J. M.; Yates, J. R.; Berry, A. J.; Wimperis, S.; Ashbrook, S. E. High-Resolution ^{19}F MAS NMR Spectroscopy: Structural Disorder and Unusual J Couplings in a Fluorinated Hydroxy-Silicate. *J. Am. Chem. Soc.* **2010**, *132*, 15651–15660.

- (19) Martineau, C.; Fayon, F.; Suchomel, M. R.; Allix, M.; Massiot, D.; Taulelle, F. Structure Resolution of $\text{Ba}_3\text{Al}_3\text{F}_{19}$ and Investigation of Fluorine Ion Dynamics by Synchrotron Powder Diffraction, Variable-Temperature Solid-State NMR, and Quantum Computations. *Inorg. Chem.* **2011**, *50*, 2644–2653.

- (20) Biswal, M.; Body, M.; Legein, C.; Sadoc, A.; Boucher, F. NbF_5 and TaF_5 : Assignment of ^{19}F NMR Resonances and Chemical Bond Analysis from GIPAW Calculations. *J. Solid State Chem.* **2013**, *207*, 208–217.

- (21) Cho, H.; de Jong, W. A.; Soderquist, C. Z. Probing the oxygen environment in UO_2^{2+} by solid-state ^{17}O nuclear magnetic resonance spectroscopy and relativistic density functional calculations. *J. Chem. Phys.* **2010**, *132*, 084501.
- (22) Smith, A. L.; Raison, P. E.; Martel, L.; Charpentier, T.; Farnan, I.; Prieur, D.; Hennig, C.; Scheinost, A. C.; Konings, R. J. M.; Cheetham, A. K. A ^{23}Na Magic Angle Spinning Nuclear Magnetic Resonance, XANES, and High-Temperature X-ray Diffraction Study of Na_2UO_4 , Na_4UO_6 , and $\text{Na}_2\text{U}_2\text{O}_7$. *Inorg. Chem.* **2014**, *53*, 375–382.
- (23) Alam, T. M.; Liao, Z.; Nyman, M.; Yates, J. Insight into Hydrogen Bonding of Uranyl Hydroxide Layers and Capsules by Use of ^1H Magic-Angle Spinning NMR Spectroscopy. *J. Phys. Chem. C* **2016**, *120*, 10675–10685.
- (24) Marchenko, A.; Truflandier, L. A.; Autschbach, J. Uranyl Carbonate Complexes in Aqueous Solution and Their Ligand NMR Chemical Shifts and ^{17}O Quadrupolar Relaxation Studied by ab Initio Molecular Dynamics. *Inorg. Chem.* **2017**, *56*, 7384–7396.
- (25) Gendron, F.; Sharkas, K.; Autschbach, J. Calculating NMR Chemical Shifts for Paramagnetic Metal Complexes from First-Principles. *J. Phys. Chem. Lett.* **2015**, *6*, 2183–2188.
- (26) Gendron, F.; Pritchard, B.; Bolvin, H.; Autschbach, J. Magnetic Resonance Properties of Actinyl Carbonate Complexes and Plutonyl-(VI)-tris-nitrate. *Inorg. Chem.* **2014**, *53*, 8577–8592.
- (27) Smiles, D. E.; Wu, G.; Hrobárik, P.; Hayton, T. W. Use of ^{77}Se and ^{125}Te NMR Spectroscopy to Probe Covalency of the Actinide-Chalcogen Bonding in $[\text{Th}(\text{E}_n)\{\text{N}(\text{SiMe}_3)_2\}_3]^-$ (E = Se, Te; $n = 1, 2$) and their Oxo-Uranium(VI) Congeners. *J. Am. Chem. Soc.* **2016**, *138*, 814–825.
- (28) Wani, B. N.; Patwe, S. J.; Rao, U. R. K.; Venkateswarlu, K. S. Fluorination of oxides of uranium and thorium by ammonium hydrogenfluoride. *J. Fluorine Chem.* **1989**, *44*, 177–185.
- (29) Capelli, E.; Beneš, O.; Beilmann, M.; Konings, R. J. M. Thermodynamic investigation of the $\text{LiF}-\text{ThF}_4$ system. *J. Chem. Thermodyn.* **2013**, *58*, 110–116.
- (30) Bureau, B.; Silly, G.; Buzaré, J. Y.; Emery, J. Superposition model for ^{19}F isotropic chemical shift in ionic fluorides: from basic metal fluorides to transition metal fluoride glasses. *Chem. Phys.* **1999**, *249*, 89–104.
- (31) Segall, M. D.; Lindan, P. J. D.; Probert, M. J.; Pickard, C. J.; Hasnip, P. J.; Clark, S. J.; Payne, M. C. First-Principles Simulation: Ideas, Illustrations and the CASTEP Code. *J. Phys.: Condens. Matter* **2002**, *14*, 2717–2744.
- (32) Clark, S. J.; Segall, M. D.; Pickard, C. J.; Hasnip, P. J.; Probert, M. I. J.; Refson, K.; Payne, M. C. First Principles Methods using CASTEP. *Z. Kristallogr.—Cryst. Mater.* **2005**, *220*, 567–570.
- (33) *Amsterdam Density Functional (ADF), SCM Theoretical Chemistry*; Vrije Universiteit: Amsterdam, The Netherlands, 2017. <http://www.scm.com>.
- (34) te Velde, G.; Bickelhaupt, F. M.; Baerends, E. J.; Fonseca Guerra, C.; van Gisbergen, S. J. A.; Snijders, J. G.; Ziegler, T. Chemistry with ADF. *J. Comput. Chem.* **2001**, *22*, 931–967.
- (35) Body, M.; Silly, G.; Legein, C.; Buzaré, J.-Y. Cluster Models and ab Initio Calculations of ^{19}F NMR Isotropic Chemical Shifts for Inorganic Fluorides. *J. Phys. Chem. B* **2005**, *109*, 10270–10278.
- (36) Alkan, F.; Holmes, S. T.; Dybowski, C. Role of Exchange and Relativistic Approximations in Calculating ^{19}F Magnetic Shielding in Solids Using a Cluster Ansatz. *J. Chem. Theory Comput.* **2017**, *13*, 4741–4752.
- (37) Martel, L.; Magnani, N.; Vigier, J.-F.; Boshoven, J.; Selfslag, C.; Farnan, I.; Griveau, J.-C.; Somers, J.; Fanghänel, T. High-resolution solid-state oxygen-17 NMR of actinide-bearing compounds: an insight into the 5f chemistry. *Inorg. Chem.* **2014**, *53*, 6928–6933.
- (38) Souček, P.; Beneš, O.; Claux, B.; Capelli, E.; Ougier, M.; Tyrpekl, V.; Vigier, J.-F.; Konings, R. J. M. Synthesis of UF_4 and ThF_4 by HF gas fluorination and re-determination of the UF_4 melting point. *J. Fluorine Chem.* **2017**, *200*, 33–40.
- (39) Rand, M.; Fuger, J.; Grenthe, I.; Neck, V.; Raiou, D. *Chemical Thermodynamics of Thorium*; Chemical Thermodynamics Series; OECD Nuclear Energy Agency, Data Bank: Issy-les-Moulineaux, France, 2009; Vol. 11, p 198.
- (40) Roinsel, T.; Rodriguez-Carvajal, J. WinPLOTR: a Windows tool for powder diffraction patterns analysis Materials Science Forum. In *Proceedings of the Seventh European Powder Diffraction Conference (EPDIC 7)*; Delhez, R., Mittenmeijer, E. J., Eds., 2000; pp 118–123.
- (41) Martel, L.; Somers, J.; Berkmann, C.; Koepp, F.; Rothermel, A.; Pauvert, O.; Selfslag, C.; Farnan, I. A nuclear magnetic resonance spectrometer concept for hermetically sealed magic angle spinning investigations on highly toxic, radiotoxic, or air sensitive materials. *Rev. Sci. Instrum.* **2013**, *84*, 055112.
- (42) Sadoc, A.; Body, M.; Legein, C.; Biswal, M.; Fayon, F.; Rocquefelte, X.; Boucher, F. ^{19}F NMR Parameters in Alkali, Alkaline Earth and Rare Earth Fluorides from First Principle Calculations. *Phys. Chem. Chem. Phys.* **2011**, *13*, 18539–18550.
- (43) Massiot, D.; Fayon, F.; Capron, M.; King, I.; Le Calvé, S.; Alonso, B.; Durand, J.-O.; Bujoli, B.; Gan, Z.; Hoatson, G. Modelling one- and two-dimensional solid-state NMR spectra. *Magn. Reson. Chem.* **2002**, *40*, 70–76.
- (44) Haerberlen, U. In *Advances in Magnetic Resonance*; Waugh, J. S., Ed.; Academic Press: New York, 1976; Suppl. 1.
- (45) Mehring, M. *Principles of High Resolution NMR in Solids*, 2nd ed.; Springer Verlag: Berlin, 1983.
- (46) Spiess, H. W. In *NMR Basic Principles and Progress*; Diehl, P., Fluck, E., Kosfeld, R., Eds.; Springer Verlag: Berlin, 1978; Vol. 15.
- (47) Yi, H.; Balan, E.; Gervais, C.; Segalen, L.; Fayon, F.; Roche, D.; Person, A.; Morin, G.; Guillaumet, M.; Blanchard, M.; Lazzeri, M.; Babonneau, F. A carbonate-fluoride defect model for carbonate-rich fluorapatite. *Am. Mineral.* **2013**, *98*, 1066–1069.
- (48) Sadoc, A.; Biswal, M.; Body, M.; Legein, C.; Boucher, F.; Massiot, D.; Fayon, F. NMR Parameters in Column 13 Metal Fluoride Compounds (AlF_3 , GaF_3 , InF_3 and TlF) from First Principle Calculations. *Solid State Nucl. Magn. Reson.* **2014**, *59–60*, 1–7.
- (49) Martineau, C.; Allix, M.; Suchomel, M. R.; Porcher, F.; Vivet, F.; Legein, C.; Body, M.; Massiot, D.; Taulelle, F.; Fayon, F. Structure Determination of $\text{Ba}_3\text{AlF}_{13}$ by Coupling Electron, Synchrotron and Neutron Powder Diffraction, Solid-State NMR and Ab Initio Calculations. *Dalton Trans.* **2016**, *45*, 15565–15574.
- (50) Perdew, J. P.; Burke, K.; Ernzerhof, M. Generalized Gradient Approximation Made Simple. *Phys. Rev. Lett.* **1996**, *77*, 3865–3868.
- (51) Pfrommer, B. G.; Côté, M.; Louie, S. G.; Cohen, M. L. Relaxation of crystals with the quasi-newton method. *J. Comput. Phys.* **1997**, *131*, 233–240.
- (52) van Lenthe, E.; Baerends, E. J.; Snijders, J. G. Relativistic total energy using regular approximations. *J. Chem. Phys.* **1994**, *101*, 9783–9792.
- (53) Gritsenko, O. V.; Schipper, P. R. T.; Baerends, E. J. Approximation of the exchange-correlation Kohn-Sham potential with a statistical average of different orbital model potentials. *Chem. Phys. Lett.* **1999**, *302*, 199–207.
- (54) Schipper, P. R. T.; Gritsenko, O. V.; van Gisbergen, S. J. A.; Baerends, E. J. Molecular calculations of excitation energies and (hyper)polarizabilities with a statistical average of orbital model exchange-correlation potentials. *J. Chem. Phys.* **2000**, *112*, 1344–1352.
- (55) Van Lenthe, E.; Baerends, E. J. Optimized Slater-type basis sets for the elements 1–118. *J. Comput. Chem.* **2003**, *24*, 1142–1156.
- (56) Inorganic Crystal Structure Database (ICSD). *ICSD Web Version 3.7.0 (Build 20171204-1045)—Data Release 2017.2*; FIZ Karlsruhe, 2017. http://www2.fiz-karlsruhe.de/icsd_home.html.
- (57) Kern, S.; Hayward, J.; Roberts, S.; Richardson, J. W., Jr.; Rotella, F. J.; Soderholm, L.; Cort, B.; Tinkle, M.; West, M.; Hoisington, D.; Lander, G. H. Temperature Variation of the Structural Parameters in Actinide Tetrafluorides. *J. Chem. Phys.* **1994**, *101*, 9333–9337.
- (58) Kepert, D. L. *Inorganic Stereochemistry*; Inorganic Chemistry Concepts; Springer-Verlag, 1982; Vol. 6.
- (59) Martineau, C.; Body, M.; Legein, C.; Silly, G.; Buzaré, J.-Y.; Fayon, F. Multinuclear High-Resolution NMR Study of Compounds

from the Ternary System NaF-CaF₂-AlF₃: from Determination to Modeling of NMR Parameters. *Inorg. Chem.* **2006**, *45*, 10215–10223.

(60) Biswal, M.; Body, M.; Legein, C.; Corbel, G.; Sadoc, A.; Boucher, F. Structural Investigation of α - and β -Sodium Hexafluoroarsenate, NaAsF₆, by Variable Temperature X-ray Powder Diffraction and Multinuclear Solid-State NMR, and DFT Calculations. *J. Phys. Chem. C* **2012**, *116*, 11682–11693.

(61) Body, M.; Silly, G.; Legein, C.; Buzaré, J.-Y. Correlation between ¹⁹F Environment and Isotropic Chemical Shift in Barium and Calcium Fluoroaluminates. *Inorg. Chem.* **2004**, *43*, 2474–2485.

(62) Shannon, R. D. Revised Effective Ionic Radii and Systematic Studies of Interatomic Distances in Halides and Chalcogenides. *Acta Crystallogr., Sect. A: Cryst. Phys., Diffr., Theor. Gen. Crystallogr.* **1976**, *32*, 751–767.

(63) Laskowski, R.; Blaha, P.; Tran, F. Assessment of DFT functionals with NMR chemical shifts. *Phys. Rev. B: Condens. Matter Mater. Phys.* **2013**, *87*, 195130.

(64) Rollet, A.-L.; Allix, M.; Veron, E.; Deschamps, M.; Montouillout, V.; Suchomel, M. R.; Suard, E.; Barre, M.; Ocaña, M.; Sadoc, A.; Boucher, F.; Bessada, C.; Massiot, D.; Fayon, F. Synthesis and Structure Resolution of RbLaF₄. *Inorg. Chem.* **2012**, *51*, 2272–2282.

(65) Martineau, C.; Legein, C.; Body, M.; Péron, O.; Boulard, B.; Fayon, F. Structural investigation of α -LaZr₂F₁₁ by coupling X-ray powder diffraction, ¹⁹F solid state NMR and DFT calculations. *J. Solid State Chem.* **2013**, *199*, 326–333.